PCCP

Accepted Manuscript

ROYAL SOCIETY OF CHEMISTRY

www.rsc.org/pccp

Enhanced Photocatalytic performance of Ag_3PO_4 Photocatalyst via Fullerene Modification: First-Principles Study

Cai-Yun Luo[1], Wei-Qing Huang[1*], Liang Xu [2, 1], Yin-Cai Yang[1], Xiaofan Li[1$], Wangyu Hu[2], P. Peng[2], and Gui-Fang Huang[1#]

[1] Department of Applied Physics, School of Physics and Electronics, Hunan University, Changsha 410082, China

[2] School of Materials Science and Engineering, Hunan University, Changsha 410082, China

Abstract

Coupling of carbon nanomaterials with semiconductor photocatalysts is a promising route to improve their photocatalytic performance. Herein, density functional theory is used to investigate electronic structure, charge transfer, photocatalytic activity and stability in a series of hybrid fullerene (C_{20}, Li@C_{20}, C_{26}, Li@C_{26})/Ag_3PO_4(100) composites. When Li atom is incorporated in fullerene, the adsorption energies significantly increase, although the change of interface distance is negligibly small due to the weak interface interaction. The charge transfer between constituents decreases with the C atom number of fullerene. Compared to pure Ag_3PO_4, the band gap of the composites is smaller, which can enhance the visible light absorption and photoinduced electrons transfer. Most importantly, a type-II, staggered band alignment can be obtained in the C_{26}-Ag_3PO_4(Li@C_{26}-Ag_3PO_4) interface, leading to significantly reduced charge recombination and thus enhanced photocatalytic activity. These results reveal that fullerene modification would be an effective strategy to improve the photocatalytic performance of Ag_3PO_4 semiconductor photocatalysts.

Keywords: Fullerene; Semiconductor photocatalysts; Photocatalytic performance; First-Principles

*. Corresponding author. *E-mail addresses:* wqhuang@hnu.edu.cn

$. Corresponding author. *E-mail:* yueyanglxf@hnu.edu.cn

#. Corresponding author. *E-mail address:* gfhuang@hnu.edu.cn

1. Introduction

Photocatalysis is a promising technology to address problems in chemical synthesis, energy utilization, and environmental remediation, such as producing hydrogen via water splitting and degrading organic pollutants. Most photocatalytic semiconductors (metal oxides, nitrides, or sulfides [1-3]) generally have wide energy gap and rapid recombination of photogenerated charge carriers, which limit their practical application. For example, TiO_2 has generally been known to be the most promising photocatalyst for the degradation of environment pollutants and the photoelectrochemical conversion of solar energy due to its relatively high efficiency, excellent chemical stability, low cost, nontoxicity. However, two crucial problems, that is, narrow lightresponse range caused by its wide band gap of 3.2 eV and low quantum efficiency induced by the fast recombination of photogenerated electron–hole pairs, impede its widespread practical applications [4, 5]. Therefore, the development of photocatalysts with high performance under visible (vis-) light irradiation would be very desirable.[6]

Recently, significant attention has been paid to silver orthophosphate (Ag_3PO_4), a new vis-light photocatalyst with extremely high photooxidative capability for O_2 generation from water splitting and superior photodegradation rate of organic dyes that is dozens of times faster than that over commercial $TiO_{2-x}N_x$ under visible light irradiation. Particularly, it's remarkable quantum yield of up to 90% indicates that Ag_3PO_4 has very low recombination rates of photoexcited carriers, making it to be one of the most promising photocatalysts in harvesting solar energy for environmental purification and clean energy production. The low structural stability of pure Ag_3PO_4 is, unfortunately, the major obstacle for its practical applications [7, 8]. To increase not only the stability but also photocatalytic activity of pure Ag_3PO_4, coupling Ag_3PO_4 with other materials has been demonstrated to be an effective strategy [9, 10]. Many Ag_3PO_4-based composites, such as Ag_3PO_4/graphene, Ag_3PO_4/CeO_2, Ag_3PO_4/AgI, Ag_3PO_4/Fe_3O_4, Ag_3PO_4/SnO_2, Ag_3PO_4/TiO_2, display enhanced stability and photocatalytic activity [11-14].

Carbon is well known to form distinct solid state allotropes with diverse structures and properties ranging from sp^3 hybridized diamond to sp^2 hybridized graphite [15, 16]. Among them, carbon nanomaterials, composed entirely of sp^2 bonded graphitic carbon, are found in all reduced dimensionalities including zero-dimensional fullerene, one-dimensional carbon nanotubes (CNTs),

and two-dimensional graphene. Their unique physical and chemical properties have inspired comprehensive studies on them due to their great potential for various potential applications [17, 18]. In particular, carbon nanomaterials are found to be very effective candidates to form nanocomposites with semiconductors, thus enhancing their photocatalytic performance. For examples, carbon nanodot-carbon nitride (C_3N_4) nanocomposite displays impressive performance for photocatalytic solar water splitting [17]. Graphene/g-C_3N_4 composites have enhanced visible-light photocatalytic activity, especially for H_2-production activity [19-23]. Graphene, CNTs and fullerene have also been used to interface with TiO_2 to enhance visible-light photocatalytic activity well than pure TiO_2 materials [24-27]. The enhanced photocatalytic performance of semiconductor/carbon composites is generally attributed to the electron-accepting and transport properties of carbon nanomaterials because they provide a convenient way to direct the flow of photogenerated charge carriers.

Density functional theory (DFT) has been used to explore the underlying mechanisms for superior photocatalytic performance of semiconductor/carbon composites. It has been demonstrated that coupling carbon nanomaterials can reduce the band gap of semiconductors, thus enhancing optical absorption in the visible region [28]. Interestingly, Du et al. first reported that graphene is the sensitizer for TiO_2 [29] and g-C_3N_4 [15], whereas Gao et al. found that significant charges transfer from anatase TiO_2 to graphene at the ground electronic state due to the different crystal structure [30]. The simulations by long et al. rationalized visible light photocatalytic activity of CNT/TiO_2 hybrid materials higher than that under ultraviolent irradiation and showed that the photoactivity of a semiconducting CNT decorating TiO_2 is better than that of the metallic CNT/TiO_2 system [31]. The DFT calculations suggested that C_{60}-interfaced TiO_2 in both the mechanical mixture and covalent linking cannot form an efficient photovoltaic heterojunction [32].

More recently, Ag_3PO_4/carbon-nanomaterials composites have been attracting increasing attention due to their highly efficient and stable visible light photocatalytic performances [18, 33-43]. For instance, the Ag_3PO_4/graphene composites prepared by different methods show superior photocatalytic activity under visible light [35, 42, 44]. Similarly, it is found that CNTs can enhance the photocatalytic activity and stability of Ag_3PO_4 under visible light [18, 34, 36-38, 41]. Moreover, carbon layer-wrapped Ag_3PO_4 possesses a much higher degradation rate of phenol and high stability than

pure Ag_3PO_4 under visible light [43]. Compared with graphene and CNTs, fullerene and endohedral metallofullerene have been attracted particular interest owing to their functional characteristics and potential applications in the fields of nanomaterials and biomedical science. Therefore, it is expected to improve the photocatalytic performance of Ag_3PO_4 by fullerene modification, just as the case of C_{60}/TiO_2.

In this work, the structural and electronic properties of hybrid fullerene/Ag_3PO_4 composites have been investigated using large-scale density functional theory (DFT) computations to explore the photocatalytic performance enhancing for Ag_3PO_4 by fullerene modification [45]. Here, C_{20} and C_{26} are taken as the fullerene models, motivated by their special structure and properties. The fullerene C_{20}, consisting solely of pentagons, is the smallest unconventional fullerene which breaks the ''isolated pentagon rule", while fullerene C_{26} is pure and intermediate open-shell compound. Moreover, they are well established as single oxygen sensitizers for electron donor-acceptor assemblies and applies in the field of photocatalysis. The role of fullerene in these photocatalytic systems can be speculated to be as follows: (1) it can act as an electron acceptor and minimize the electron-hole recombination, and thus provide enhanced photocatalytic activity; (2) it can also act as be an electron donor to improve the photocatalytic activity through sensitization of Ag_3PO_4. The calculated results show that the band gap can be largely reduced due to interfacing with fullerene, resulting into a strong absorption in the entire visible region and thus superior photocatalytic activity. The electrostatic potential distribution in the interface, where the potential at fullerene is higher than that in Ag_3PO_4, can effectively inhibit the reducibility of Ag^+ ions in the $Ag_3PO_4(100)$ surface and therefore improving its stability. A built-in potential formed at the interface can improve the stability of Ag_3PO_4. This work would provide some new insight into optimizing the photocatalytic properties of Ag_3PO_4-based or carbon-based nanomaterial composites.

2. Computational method

To construct the complex of Ag_3PO_4 and fullerene, we choose a stoichiometric cubic $Ag_3PO_4(100)$ slab because it is the most stable one among the low index surfaces. C_{20}, $Li@C_{20}$, C_{26}, and $Li@C_{26}$ (containing 20, 21, 26, and 27 atoms, respectively) are chosen to match a 2×2

Ag_3PO_4(100) surface slab (containing 32 O, 8 P and 24 Ag atoms) with three bottom layers fixed at bulk position. The vacuum depth is as large as 15 Å for all of the models to avoid artificial interaction in a supercell (11.78 ×11.78 × 26.32 $Å^3$). Note that there is no tensile or compressed deformation of Ag_3PO_4(100) surface in the *xy* plane, different from other models (CeO_2/GR [46], g-C_3N_4/GR [19], TiO_2/CNT [24], $SrTiO_3$/GR [47]). The local density approximation (LDA) with inclusion of the van der Waals (vdW) interaction is chosen because long-range vdW interactions are expected to be significant in such these complexes. However, LDA has been known generally to underestimate the energy gap of semiconductor, resulting into an overestimate for photoinduced electrons transfer in photocatalytic process. To correct this band gap problem, all of the theoretical calculations are performed using the DFT/LDA+U method implemented in the plane wave basis CASTEP code. We performed extensive tests to determine the appropriate U parameters for Ag 4d states, which reproduced the correct energy gap (2.48 eV) for cubic Ag_3PO_4. The appropriate Hubbard U values for Ag 4d, O 2p, and P 3p are 7.2, 7.0, and 7.0 eV, respectively. A Morkhost-Pack mesh of k points, 2 × 2 × 1 and 4 × 4 × 1 points, is used, respectively, to sample the two-dimensional Brillouin zone for geometry optimization and for calculating the density of states. The cutoff energy for plane waves is chosen to be 400 eV, and the convergence tolerance of force on each atom during structure relaxation is set at 0.01 eV/Å.

The strong light absorption is one of fundamental premises for a high-efficiency photocatalyst. The dielectric function of the semiconductor materials is mainly connected with the electronic response. The frequency-dependent dielectric matrix is calculated pure Ag_3PO_4, Ag_3PO_4(100) surface, and hybrid fullerene (C_{20}, Li@C_{20}, C_{26}, Li@C_{26})/Ag_3PO_4 systems by the Fermi golden rule within the dipole approximation. The imaginary part ε_2 of the dielectric function, ε is calculated from the momentum matrix elements between the occupied and unoccupied wave functions, given by:

$$\varepsilon_2 = \frac{ve^2}{2\pi\hbar m^2\omega^2}\int d^3k \sum_{n,n'}|\langle kn|p|kn'\rangle|^2 f(kn)(1-f(kn'))\delta(E_{kn}-E_{kn'}-\hbar\omega) \qquad (1)$$

where $\hbar\omega$ is the energy of the incident photon, p is the momentum operator $r(\hbar/i)(\partial/\partial x)$, $(|kn\rangle)$ is a crystal wave function and $f(kn)$ is Fermi function. The imaginary part $\varepsilon_2(\omega)$ of the dielectric function could be calculated from the momentum matrix elements between the occupied and unoccupied wave functions with the selection rules, and the

real part $\varepsilon_1(\omega)$ of the dielectric function can be evaluated from imaginary part by the Kramer–Kronig relationship. The optical absorption coefficient I(ω) can be obtained as follows:

$$I(\omega) = \sqrt{2}\omega\left[\sqrt{\varepsilon_1^2(\omega) + \varepsilon_2^2(\omega)} - \varepsilon_1(\omega)\right]^{1/2} \quad (2)$$

Taking into account the tensor nature of the dielectric function, $\varepsilon_1(\omega)$ and $\varepsilon_2(\omega)$ are averaged over three polarization vectors (along x, y, and z directions). All other optical constants can also be obtained. The relations above are the theoretical basis of band structure and optical properties analyzing which reflected the mechanism of absorption spectral caused by electronic transition between different energy levels.

3. Results and discussion

3.1. Geometric Structure and Electronic Properties

Three representatives of models are illustrated in Figure 1: Parts a and b respectively present the top and side views of the simulating interface between C_{20} and the cubic $Ag_3PO_4(100)$ surface models, part c displays side view of the hybrid $Li@C_{26}/Ag_3PO_4(100)$ model used in our calculations. Geometry optimizations have first been performed for all of the systems using the conjugate gradient method. The equilibrium distances between the fullerene and the top layer of $Ag_3PO_4(100)$ surface are calculated to be 3.06, 3.07, 2.62, and 2.67 Å for $C_{20}/Ag_3PO_4(100)$, $Li@C_{20}/Ag_3PO_4(100)$, $C_{26}/Ag_3PO_4(100)$, and $Li@C_{26}/Ag_3PO_4(100)$ (as listed in table 1), which is about equal to those between the GR sheet and other materials (2.65 Å and 2.62 Å for $GR/TiO_2(110)$ [48], 2.85 Å for $GR/TiO_2(001)$ [49], 2.42-2.87 Å for GR/ZnO(0001) [50]). The smaller interface distance shows that the interface interaction between C_{26} and $Ag_3PO_4(100)$ surface is stronger than that between C_{20} and $Ag_3PO_4(100)$ surface, due to more C atoms near the $Ag_3PO_4(100)$ surface in the former. Li atom embedded in the fullerene decreases the interface interaction slightly. After optimization, the fullerene and $Ag_3PO_4(100)$ surface are nearly unchanged, indicating that the fullerene/$Ag_3PO_4(100)$ interaction is indeed vdW rather than covalent, in accordance with the others' results [28, 39]. Closer inspection of the atomic position at the interface reveals that, due to the interface interaction between $Ag_3PO_4(100)$ surface and fullerene, the Ag atoms in the top layer just under fullerene are pushed downward about 0.25 and 0.28 Å by C_{20} and $Li@C_{20}$, respectively; whereas the O atoms near fullerene slightly move

downward about 0.03 Å. In the $C_{26}/Ag_3PO_4(100)$ and $Li@C_{26}/Ag_3PO_4(100)$ composites, however, the corresponding Ag atoms only move about 0.03 and 0.06 Å, respectively, and those O atoms about 0.02 Å. The displacement discrepancy of the atoms in the top layer of $Ag_3PO_4(100)$ surface demonstrates that the interface interaction depends on the carbon number of fullerene. The rearrangements of atoms in the top layer of $Ag_3PO_4(100)$ surface indicate that the electron transfer occurs at the interface, which will be discussed later.

The stability of the hybrid fullerene/Ag_3PO_4 composites can be assessed by the interface adhesion energy, which is defined as:

$$E_{ad} = E_{comb} - E_{fullerene} - E_{Ag_3PO_4(100)} \quad (3)$$

where E_{comb}, $E_{fullerene}$, and $E_{Ag_3PO_4(100)}$ represent the total energy of the relaxed fullerene/$Ag_3PO_4(100)$, pure fullerene, and clean $Ag_3PO_4(100)$ surface, respectively. By this definition, negative E_{ad} suggests that the interface is stable. The interface adhesion energy is calculated to be -2.15, -0.76, -2.39, and -0.78eV for the $C_{20}/Ag_3PO_4(100)$, $Li@C_{20}/Ag_3PO_4(100)$, $C_{26}/Ag_3PO_4(100)$, $Li@C_{26}/Ag_3PO_4(100)$ composites, respectively, which indicates a rather strong interaction between fullerene and $Ag_3PO_4(100)$ surface, and the high thermodynamically stability of these composites. Compared with the $C_{20}/Ag_3PO_4(100)$ composite, the $C_{26}/Ag_3PO_4(100)$ composite with lower adhesion energy can form more easily, in line with its smaller interface distance. The encapsulation of Li atom in the fullerene is not seem conducive to the formation of composites.

3.2. Density of states

To explore the effect of fullerene adhered on the electronic properties of $Ag_3PO_4(100)$, we have calculated the density of states (DOSs) of individual $Ag_3PO_4(100)$ surface, fullerene, and their hybrids, as shown in Figure 2. Pure Ag_3PO_4 is an indirect semiconductor with a band gap (E_g) of 2.45 eV [51]. Due to its very dispersive of the bottom of conduction band (CB), the photogenerated electrons in pure Ag_3PO_4 possess smaller effective masses, which promote the separation of electron-hole pairs during the reaction process, thus leading to its good photocatalytic activity [52]. As its $Ag_3PO_4(100)$ surface is exposed, Ag_3PO_4 becomes a direct band gap semiconductor [39] and the E_g decreases to 2.15 eV, as shown in Figure 2(a1). The valence band maximum (VBM) is

derived from O 2p, mixing with small Ag 4d states. Above the Fermi level, the conduction band minimum (CBM) is dominated by Ag 5s states, which form the anti-bonding state. The calculated DOSs show that energy gaps for individual C_{20}, Li@C_{20}, C_{26}, and Li@C_{26} are 1.95, 2.07, 1.71, and 1.83 eV, respectively (Figures 2 (a2-a5)), which the first and third ones are agree well with the theoretical values of 1.94 and 1.60 eV [53, 54], respectively. Obviously, excitation of an electron from the lowest unoccupied molecular orbital (LUMO) of the fullerene to the highest occupied molecular orbital (HOMO) requires much lower energy than in Ag_3PO_4. Figure a2 (a5) displays that introduction of Li into C_{20} (C_{26}) breaks the degeneracy of the C_{20} (C_{26}) HOMO (LUMO), indicating that the influence of Li atom on the electronic properties of the fullerene is related with the carbon number. It also demonstrates that Li states mix well with the CB of C_{20} (C_{26}). The orbital hybrid is beneficial for Li donating an electron to C_{20} (C_{26}) and enhances intermolecular electrostatic interactions compared to pristine C_{20} (C_{26}).

The calculated DOSs of the above four composites characterize the interface electronic properties and energy levels alignment in detail, as shown in Figures 2 (b1)-(b4) and Table 1. One can see that the each component of the combined DOS changes slightly compared to the individual DOSs (Figures 2 (a1)-(a5)), indicating that the interface interaction is indeed weak. The calculated band gaps of four composites are 1.92, 2.04, 0.78, and 0.66 eV, respectively, as listed in Table 1. The reduced band gaps can make the composites absorb the most sunlight, and the photogenerated electron transfer from the valence band (VB) to the conduction band (CB) of the fullerene/Ag_3PO_4(100) composites becomes easier, leading to the red shift of the optical absorption edge, thus enhancing the photocatalytic performance. For the Li@C_{20}/Ag_3PO_4(100) composite, the introduction of Li atom in C_{20} slightly reduces the band gap. Similarly, Li atom also leads to the reduction of the band gap of the Li@C_{26}/Ag_3PO_4(100) composite. This is because Li states mix with the CB of C_{20} and C_{26} at different energy regions (Figures 2 (b2) and (b4)). Interestingly, the CB bottom is only consisted of states from C_{20} (Li@C_{20}, C_{26}, Li@C_{26}) which greatly broadens the CB bottom of the fullerene/Ag_3PO_4(100) composites. However, the upper part of VB of the fullerene/Ag_3PO_4(100) composites shows complex types. For the C_{26}/Ag_3PO_4(100) and Li@C_{26}/Ag_3PO_4(100) composite, the upper part of VB is formed from Ag 4d, mixing with small P 3p and O 2p orbits, which can be more clearly seen from the electron

density distributions of the highest occupied and lowest unoccupied levels (HOL and LUL), respectively, as shown in Figure 3. More importantly, the interfaces of $C_{26}/Ag_3PO_4(100)$ and $Li@C_{26}/Ag_3PO_4(100)$ composites are type II (see Figures 3(c1) (d1) and (c2) (d2)), namely, with both the valence and conduction band edges of $C_{26}(Li@C_{26})$ below the corresponding Ag_3PO_4 counterparts, which significantly lowers the effective band gap of the composite and facilitates efficient electron-hole separation. As Li atom is embedded in C_{26}, however, the HOL is composed of the Ag 4d states mixed with O 2p and P 3p states delocalized near the top layer of $Ag_3PO_4(100)$ surface (Figures 3(d1)). Figures 3 (a1) and (b1) clearly displays that the HOL is only composed of the C 2p states. In photocatalysis, such band alignment is not beneficial for the separation of electron-hole pairs. Thus, the fullerene would be a sensitizer for Ag_3PO_4. These results indicate that choosing appropriate fullerene (such as C_{26} or $Li@C_{26}$) is especially critical to obtain high efficiency of electron-hole separation in the fullerene/$Ag_3PO_4(100)$ composites.

3.2. Charge Density Difference and Mechanism Analysis.

The interaction between Ag_3PO_4 and fullerene implies a substantial charge transfer between the involved constituents. This can be visualized (as shown in Figure 4) by three-dimensional charge density difference $\Delta\rho = \rho_{fullerene/Ag_3PO_4} - \rho_{Ag_3PO_4} - \rho_{fullerene}$, where $\rho_{fullerene/Ag_3PO_4}$, $\rho_{Ag_3PO_4}$ and $\rho_{fullerene}$ are the charge densities of the composites, the $Ag_3PO_4(100)$ surface and fullerene in the same configuration, respectively. Figure 4 displays that charge redistribution mostly takes place at the fullerene/Ag_3PO_4 interface region and relaxes a bit into Ag_3PO_4 bulk states, whereas can be seen in the whole fullerene species, especially at the bottom layer C atoms in the fullerene. This shows that the effect of interface interaction on charge redistribution of fullerene is much bigger than that in Ag_3PO_4. A strong charge accumulation (blue part in Figure 4), mainly from the bottom layer C atoms of the fullerene (facing the surface) and some from the charge loosed by Ag atoms along the *z* axis just under the C atom rings, is found just above the Ag atoms in the top layer. Moreover, the charge redistribution at the interface becomes more significant as the carbon number is increased (comparing Figures 4(a) with (d)), which is consistent with the shorter interface distance and stronger interaction. But unexpectedly, Li atom embedded in C_{20} (C_{26}) has no evident effect on the charge redistribution at interface of these fullerene/Ag_3PO_4 composites (Figures 4 (c) and (f)).

Part e of Figure 4 plots is the planar averaged charge density difference along the direction perpendicular to the $Ag_3PO_4(100)$ surface, which offers quantitative results of charge redistribution. The positive values represent electron accumulation, and negative values indicate electron depletion. One can see that the largest efficient electron accumulation localized above the Ag atoms in the top layer is about 5.3 (5.4) × 10^{-4} e/Å^3 in the C_{20} (Li@C_{20})/$Ag_3PO_4(100)$ composites, and 6.1 × 10^{-4} e/Å^3 in the C_{26} (Li@C_{26})/$Ag_3PO_4(100)$ composites; while the largest local efficient electron depletion at the lowest layer C atoms is about -4.0 × 10^{-4} e/Å^3 in the C_{20} (Li@C_{20})/$Ag_3PO_4(100)$ composites. Figure 4(e) shows that there is efficient electron accumulation at the top layer of $Ag_3PO_4(100)$ surface in the C_{20} (Li@C_{20})/$Ag_3PO_4(100)$ composites; by contrast, the efficient electron depletion can be observed at the top layer of $Ag_3PO_4(100)$ surface in the C_{26} (Li@C_{26})/$Ag_3PO_4(100)$ composites. This indicates that the fullerene with more C atoms has more attractive to electrons, which is beneficial to enhancing the stability of Ag_3PO_4 photocatalyst. This plot further depicts that the charge redistribution effect of Li atom embedded is more apparent at interface of the C_{26} (Li@C_{26})/$Ag_3PO_4(100)$ composites compared to the C_{20} (Li@C_{20})/$Ag_3PO_4(100)$ composites.

To quantitatively analyze the charge variation at the interface, the Mulliken population analysis of the plane-wave pseudopotential calculations has been performed on the fullerene, $Ag_3PO_4(100)$ surface, and fullerene/$Ag_3PO_4(100)$ composites. Figure 5 shows the results of the Mulliken charge on different atoms, in which several typical values are denoted. The 3-fold coordinated O at the top layer of $Ag_3PO_4(100)$ surface has a Mulliken charge of -1.0, while those become -0.97, -0.97, -0.96, and -0.95 in the C_{20}/$Ag_3PO_4(100)$, Li@C_{20}/$Ag_3PO_4(100)$, C_{26}/$Ag_3PO_4(100)$, and Li@C_{26}/$Ag_3PO_4(100)$ composites, respectively, indicating that the electron of O atoms at the top layer of $Ag_3PO_4(100)$ surface is reduced due to the coupling of fullerene. The 2-fold coordinated Ag in the top layer of $Ag_3PO_4(100)$ surface and fullerene/$Ag_3PO_4(100)$ composite have a Mulliken charge of +0.58 and +0.63, +0.57 (C_{20}/$Ag_3PO_4(100)$), +0.61, +0.57 (Li@C_{20}/$Ag_3PO_4(100)$), +0.74, +0.58 (C_{26}/$Ag_3PO_4(100)$), +0.69, +0.58 (Li@C_{26}/$Ag_3PO_4(100)$), respectively. The charge variation demonstrates that the Ag atoms in the top layer of the C_{26} (Li@C_{26})/$Ag_3PO_4(100)$ composite would lose more electrons than those in pure $Ag_3PO_4(100)$ surface. This would improve the stability of fullerene/Ag_3PO_4 photocatalyst, just as the case of

GR/Ag_3PO_4 [39]. Although the C atom in the fullerene has a Mulliken charge of approach zero electrons, those C atoms in the fullerene/Ag_3PO_4(100) composite have different Mulliken charges because not only the arrangement of atoms under various C atoms is different, but also the interface interaction is varied. For example, Figure 5(a) shows that, in the C_{20}/Ag_3PO_4(100) composite, the C atom directly over the Ag atom has a Mulliken charge of -0.07, and its next one has a Mulliken charge of -0.05, whereas the C atom right above the O atom has a Mulliken charge of 0.01. Those C atoms at the corresponding to positions in the $Li@C_{20}/Ag_3PO_4$(100) composite have a Mulliken charge of -0.12, -0.11, and -0.08, respectively, which are partly come from Li atom. For the C_{26} ($Li@C_{26}$)/Ag_3PO_4(100) composite, it is similar to the case of C_{20}($Li@C_{20}$)/Ag_3PO_4(100) composite. As a result, the charge distribution fluctuations appear at the bottom layer C atoms due to the interactions between fullerene and Ag_3PO_4(100) surface. This might be attributed to the different atom configurations in the interface (one is metal Ag atom, the other is nonmetal O atom).

The effective net charge from one constituent to another in these composites can be analyzed on the basis of the Bader method, as listed in Table 1. Interestingly, the carbon number of the fullerene determines the transfer direction of net charge: some electrons transfer from C_{20} ($Li@C_{20}$) to Ag_3PO_4(100) surface in the C_{20}($Li@C_{20}$)/Ag_3PO_4(100) composite, but it is in the opposite direction in the C_{26}($Li@C_{26}$)/Ag_3PO_4(100) composite. Moreover, the number of electrons transferred from C_{20} ($Li@C_{20}$) to Ag_3PO_4(100) surface is larger than that from Ag_3PO_4(100) surface to C_{26}($Li@C_{26}$). For example, 0.16 electron transfers from C_{20} to Ag_3PO_4(100) surface, whereas 0.04 from Ag_3PO_4(100) surface to C_{26}. Interestingly, Li atom embedded has no effect on the effective net charge transfer in the C_{20} ($Li@C_{20}$)/Ag_3PO_4(100) composite; whereas it increases from 0.04 to 0.08 in the C_{26}($Li@C_{26}$)/Ag_3PO_4(100) composite. To understand the origin of such an interface electron transfer in these composites, work functions for the fullerene and Ag_3PO_4(100) surface are calculated by aligning the Fermi level relative to the vacuum energy level. They are calculated to be 4.48, 4.58, 5.58, 5.54, and 5.46 eV for C_{20}, $Li@C_{20}$, C_{26}, $Li@C_{26}$, and Ag_3PO_4(100) surface, respectively. The spontaneous interfacial charge transfer in the fullerene/Ag_3PO_4(100) composites can be simply rationalized in terms of the difference of these work functions. Moreover, the larger difference in work functions, the more charge transfer. For

instance, the work function difference (0.98 eV) between C_{20} and $Ag_3PO_4(100)$ surface is larger than that (0.12 eV) between C_{26} and $Ag_3PO_4(100)$ surface; thus, the transfer amount of charge in the former is bigger than in the latter (0.16 vs 0.04).

The interfacial charge transfer will alter the potential distribution at interface. The profile of the planar averaged self-consistent electrostatic potential for the fullerene/$Ag_3PO_4(100)$ composites as a function of position in the z-direction is displayed in Figure 4(b). In the Ag_3PO_4 lattice, the periodic lattice potential is clear although it has some distortion due to the atoms in first four layers having a slight movement compared to their positions in bulk Ag_3PO_4. Compared to C_{20} ($Li@C_{20}$), the coupled C_{26} ($Li@C_{26}$) has more influence on the lattice potential near the surface of Ag_3PO_4. Figure 4(b) shows that the planar average electrostatic potential at the $Ag_3PO_4(100)$ surface is higher than that at the fullerene. As a consequence, a built-in potential is formed at the interface, due to the appearance of electrostatic potential difference. Under light irradiation, the separation and migration of photogenerated carriers at the interface will be affected by this built-in potential, i.e., the existence of a potential well can effectively hinder the recombination of photogenerated charge carriers in the fullerene/$Ag_3PO_4(100)$ composites. Therefore, the photocatalytic activity and stability of Ag_3PO_4 photocatalyst could be improved by coupling fullerene.

3.3. Optical Properties.

For many semiconductors (for example, TiO_2, CeO_2, $SrTiO_3$, and g-C_3N_4) with wide band gap, the incorporated GR sheet can extend their absorption edge to the vis-light region [19, 47]. Similarly, coupling fullerene with wide-band-gap semiconductors is also an effective strategy to extend the absorption edge and enhance the photocatalytic activity [55-57]. To explore the influence of the coupled fullerene on the light absorption and photocatalytic performance of Ag_3PO_4, the imaginary part of the dielectric function and UV-vis absorption spectra of pure Ag_3PO_4, $Ag_3PO_4(100)$ surface, and the fullerene/$Ag_3PO_4(100)$ composites are calculated, as shown in Figure 6. For the bulk Ag_3PO_4, the optical absorption occurs at about 2.48 eV, which is attributed to the intrinsic transition from the O 2p to Ag 5s orbitals. As the $Ag_3PO_4(100)$ surface is exposed, the absorption edge shifts to 2.15 eV due to the presence of surface states, also corresponding to the intrinsic transition. Previous investigations found that the electron transition leads to the

formation of Ag layers on the surface of Ag_3PO_4, i.e., photocorrosion, which largely limits its practical application as a recyclable highly efficient photocatalyst. Moreover, the absorption intensities of both pure Ag_3PO_4 and Ag_3PO_4(100) surface are weak in the visible-light region, as shown in Figure 6. The two serious limitations are expected to be improved by the fullerene combination. As can be clearly seen from Figure 6, the red shift of absorption edge of the fullerene/Ag_3PO_4(100) composites is obvious due to their small band gaps, compared to that of pure Ag_3PO_4 and Ag_3PO_4(100) surface. The large red shift is caused by the transition from the C 2p to Ag 5s states, or C 2p to C 2p states. Furthermore, the absorption intensity of fullerene/Ag_3PO_4(100) composites is enhanced significantly in the UV-vis light region. Miraculously the shape of absorption curve of the fullerene/Ag_3PO_4(100) composite depends on the carbon number of the fullerene (see Figure 6(b)), indicating that the electronic transitions are different. In the region from 400 to 550 nm, the absorption of C_{20} (Li@C_{20})/Ag_3PO_4(100) composite is much higher than that of C_{26} (Li@C_{26})/Ag_3PO_4(100) composite; whereas for the latter, a absorption peak appears and covers from 550 to 800 nm. These distinctions can be attributed to the difference of electronic structures, especially those near the band gap (Figures 2 and 3). Figure 6 also shows that the Li atom embedded has no apparent effect on the absorption spectra of the fullerene/Ag_3PO_4(100) composites. Thus, it is reasonable to conclude that coupling fullerene on the Ag_3PO_4 semiconductor would lead to the strong absorption in the UV-vis region, which is one of the most important factors to improve the photocatalytic activity of Ag_3PO_4.

Since 2007, fullerene has been used to couple with various semiconductors in order to improve their photocatalytic activity. For examples, C_{60}/Bi_2WO_6 [58], C_{60}/ZnO [59], C_{60}/TiO_2 [55, 60-62], C_{60}/Bi_2MoO_6 [63], C_{60}/CdSe [64], $C_{60}/Bi_2TiO_4F_2$ [65], and C_{60}/g-C_3N_4 [56, 57] photocatalysts have already been synthesized experimentally. These hybrid C_{60}/semiconductor photocatalysts have enhanced photocatalytic activity, which is attributed to the increased light absorption intensity in visible light region, and more efficient separation of the photoexcited electron-hole pairs due to the presence of C_{60} molecules. Based on these hybrid fullerene/semiconductor composites, it is

reasonable to conclude that the hybrid fullerene/Ag_3PO_4 composites, such as C_{20} (Li@C_{20}, C_{26}, Li@C_{26})/Ag_3PO_4 hybrids discussed in this work can be synthesized by the appropriate method. We expect that the hybrid fullerene/Ag_3PO_4 composites, as highly efficient visible-light-driven photocatalysts, are unique competitive candidates for energy utilization and environmental remediation, and provide insight into the feasibility of coupling organic molecules with inorganic semiconductor as novel photocatalysts.

4. Summary

In summary, we have performed a first-principles investigation on the electronic structure, charge transfer, photocatalytic activity and stability of fullerene/Ag_3PO_4(100) composites. It is unveiled that the fullerene can act as a sensitizer in Ag_3PO_4(100)-based nanocomposites to improve the photocatalytic activity and stability. Compared to pure Ag_3PO_4, the hybrid fullerene/Ag_3PO_4 nanocomposite has a smaller band gap (1.92, 2.04, 0.78, and 0.66 eV), thus extending the absorption spectrum covering the entire visible region, and even in the infrared region. The type-II, staggered, band alignment existing between the C_{26}(Li@C_{26}) and Ag_3PO_4(100) surface can promote the separation of photoinduced carriers, thus enhancing the photocatalytic activity. As Li atom is embedded in C_{20} (C_{26}), the Li donating an electron to C_{20} (C_{26}) and enhances intermolecular electrostatic interactions compared to pristine C_{20} (C_{26}). As a sensitizer, C_{26} is expected to arise in other fullerene-Ag_3PO_4 semiconductor nanocomposites. These findings provide a theoretic base for developing highly efficient Ag_3PO_4-based or fullerene-based photocatalysts.

Acknowledgements

This work was supported by the National Natural Science Foundation of China (Grant Nos. 51471068 and 51271075).

References

1. R. Asahi, T. Morikawa, T. Ohwaki, K. Aoki and Y. Taga, *Science*, 2001, **293**, 269-271.
2. X. Chen and S. S. Mao, *Chem. Rev.*, 2007, **107**, 2891-2959.
3. Z. G. Zou, J. H. Ye, K. Sayama and H. Arakawa, *Nature*, 2001, **414**, 625-627.
4. H. Pan, B. H. Gu and Z. Y. Zhang, *J. Chem. Theory Comput.*, 2009, **5**, 3074-3078.
5. X. C. Mao, X. F. Lang, Z. Q. Wang, Q. Q. Hao, B. Wen, Z. F. Ren and X. M. Yang, *J. Phys. Chem. Lett.*, 2013, **4**, 3839-3844.
6. V. Abdelsayed, S. Moussa, H. M. Hassan, H. S. Aluri, M. M. Collinson and M. S. El-Shall, *J. Phys. Chem. Lett.*, 2010, **1**, 2804-2809.
7. X. G. Ma, B. Lu, D. Li, R. Shi, C. S. Pan and Y. F. Zhu, *J. Phys. Chem. C*, 2011, **115**, 4680-4687.
8. D. J. Martin, N. Umezawa, X. W. Chen, J. H. Ye and J. W. Tang, *Energy Environ. Sci.*, 2013, **6**, 3380-3386.
9. Y. Bi, S. Ouyang, J. Cao and J. Ye, *Phys. Chem. Chem. Phys.*, 2011, **13**, 10071-10075.
10. W. F. Yao, B. Zhang, C. P. Huang, C. Ma, X. L. Song and Q. J. Xu, *J. Mater. Chem.*, 2012, **22**, 4050-4055.
11. Z. Chen, W. Wang, Z. Zhang and X. Fang, *J. Phys. Chem. C*, 2013, **117**, 19346-19352.
12. G. P. Li and L. Q. Mao, *RSC Adv.*, 2012, **2**, 5108-5111.
13. Z. M. Yang, G. F. Huang, W. Q. Huang, J. M. Wei, X. G. Yan, Y. Y. Liu and A. L. Pan, *J Mater Chem A*, 2014, **2**, 1750-1756.
14. L. L. Zhang, H. C. Zhang, H. Huang, Y. Liu and Z. H. Kang, *New J. Chem.*, 2012, **36**, 1541-1544.
15. A. J. Du, S. Sanvito, Z. Li, D. Wang, Y. Jiao, T. Liao and S. C. Smith, *J. Am. Chem. Soc.*, 2012, **134**, 4393-4397.
16. Z. B. Liu, X. Zhao, X. L. Zhang, X. Q. Yan, Y. P. Wu, Y. S. Chen and J. G. Tian, *J. Phys. Chem. Lett.*, 2011, **2**, 1972-1977.
17. J. Liu, Y. Liu, N. Y. Liu, Y. Z. Han, X. Zhang, H. Huang and Z. H. Kang, *Science*, 2015, **347**, 970-974.
18. W. Y. Zhai, G. P. Li, P. Yu, L. F. Yang and L. Q. Mao, *J. Phys. Chem. C*, 2013, **117**, 15183-15191.
19. Q. J. Xiang, J. G. Yu and M. Jaroniec, *J. Phys. Chem. C*, 2011, **115**, 7355-7363.
20. Y. J. Zhang, T. Mori, L. Niu and J. H. Ye, *Energy Environ. Sci.*, 2011, **4**, 4517-4521.
21. G. Z. Liao, S. Chen, X. Quan, H. T. Yu and H. M. Zhao, *J. Mater. Chem.*, 2012, **22**, 2721-2726.
22. Y. B. Li, H. M. Zhang, P. R. Liu, D. Wang, Y. Li and H. J. Zhao, *Small*, 2013, **9**, 3336-3344.
23. Y. Zheng, Y. Jiao, Y. H. Zhu, L. H. Li, Y. Han, Y. Chen and S. Z. Qiao, *Nat. Commun.*, 2014, **5**.
24. K. Woan, G. Pyrgiotakis and W. Sigmund, *Adv. Mater.*, 2009, **21**, 2233-2239.
25. Y. H. Zhang, Z. R. Tang, X. Z. Fu and Y. J. Xu, *Acs Nano*, 2011, **5**, 7426-7435.
26. A. Migani, D. J. Mowbray, J. Zhao, H. Petek and A. Rubio, *J. Chem. Theory Comput.*, 2014,

10, 2103-2113.

27. H. Fox, K. E. Newman, W. F. Schneider and S. A. Corcelli, *J. Chem. Theory Comput.*, 2010, **6**, 499-507.
28. J. J. Liu, X. L. Fu, S. F. Chen and Y. F. Zhu, *Appl. Phys. Lett.*, 2011, **99**, 191903.
29. A. Du, Y. H. Ng, N. J. Bell, Z. Zhu, R. Amal and S. C. Smith, *J. Phys. Chem. Lett.*, 2011, **2**, 894-899.
30. H. T. Gao, X. H. Li, J. Lv and G. J. Liu, *J. Phys. Chem. C*, 2013, **117**, 16022-16027.
31. R. Long, *J. Phys. Chem. Lett.*, 2013, **4**, 1340-1346.
32. R. Long, Y. Dai and B. B. Huang, *J. Phys. Chem. Lett.*, 2013, **4**, 2223-2229.
33. Q. H. Liang, Y. Shi, W. J. Ma, Z. Li and X. M. Yang, *Phys. Chem. Chem. Phys.*, 2012, **14**, 15657-15665.
34. J. Q. Tian, H. Y. Li, Z. C. Xing, L. Wang, A. M. Asiri, A. O. Al-Youbi and X. P. Sun, *J. Nano Res.*, 2013, **15**.
35. X. F. Yang, H. Y. Cui, Y. Li, J. L. Qin, R. X. Zhang and H. Tang, *ACS Catal*, 2013, **3**, 363-369.
36. B. Liu, Z. Y. Li, S. Xu, T. T. Cong, L. Tian, C. Y. Ding and M. Lu, *Mater. Lett.*, 2014, **131**, 229-232.
37. B. Liu, Z. Y. Li, S. Xu, D. D. Han and D. Y. Lu, *J. Alloys Compd.*, 2014, **596**, 19-24.
38. S. M. Wang, D. L. Li, C. Sun, S. G. Yang, Y. Guan and H. He, *J. Mol. Catal. A: Chem.*, 2014, **383**, 128-136.
39. L. Xu, W. Q. Huang, L. L. Wang, G. F. Huang and P. Peng, *J. Phys. Chem. C*, 2014, **118**, 12972-12979.
40. X. F. Yang, J. L. Qin, Y. Jiang, R. Li, Y. Li and H. Tang, *RSC Adv.*, 2014, **4**, 18627-18636.
41. L. Cai, T. Xu, J. Shen and W. Xiang, *Mater. Sci. Semicond. Process.*, 2015, **37**, 19-28.
42. Q. J. Xiang, D. Lang, T. T. Shen and F. Liu, *Appl. Catal., B*, 2015, **162**, 196-203.
43. Y. C. Xie, X. W. Wang and X. Wen, *Nano*, 2015, **10**.
44. O. S. Bokareva, G. Grell, S. I. Bokarev and O. Kühn, *J. Chem. Theory Comput.*, 2015, **11**, 1700-1709.
45. D. Walsh, N. M. Sanchez-Ballester, K. Ariga, A. Tanaka and M. Weller, *Green Chem.*, 2015, **17**, 982-990.
46. L. Xu, W. Q. Huang, L. L. Wang and G. F. Huang, *ACS Appl. Mater. Interfaces*, 2014, **6**, 20350-20357.
47. Y. C. Yang, L. Xu, W. Q. Huang, C. Y. Luo, G. F. Huang and P. Peng, *J. Phys. Chem. C*, 2015, **119**, 19095-19104.
48. X. H. Li, H. T. Gao and G. J. Liu, *J. Chem. Theory Comput.*, 2013, **1025**, 30-34.
49. W. J. Ong, L. L. Tan, S. P. Chai, S. T. Yong and A. R. Mohamed, *Nano Res.*, 2014, **7**, 1528-1547.
50. H. G. Fan, X. T. Zhao, J. H. Yang, X. N. Shan, L. L. Yang, Y. J. Zhang and M. Gao, *Catal. Commun.*, 2012, **29**, 29-34.
51. Z. G. Yi, J. H. Ye, N. Kikugawa, T. Kako, S. X. Ou Yang, H. Stuart-Williams and R. L. Withers, *Nat. Mater.*, 2010, **9**, 559-564.
52. N. Umezawa, O. Y. Shu Xin and J. H. Ye, *Phys. Rev. B: Condens. Matter*, 2011, **83**, 035202.
53. J. An, L. H. Gan, J. Q. Zhao and R. Li, *J. Chem. Phys.*, 2010, **132**, 154304.
54. Y. Cao, D. Wang, B. Liu, G. Yao, Y. Fu, X. Li and Z. Bi, *Int. J. Quantum Chem.*, 2013, **113**, 1440-1446.

55. W. C. Oh, F. J. Zhang and M. L. Chen, *J. Ind. Eng. Chem.*, 2010, **16**, 299-304.
56. X. J. Bai, L. Wang, Y. J. Wang, W. Q. Yao and Y. F. Zhu, *Appl. Catal., B*, 2014, **152-153**, 262-270.
57. B. Chai, X. Liao, F. Song and H. Zhou, *Dalton Trans.*, 2014, **43**, 982-989.
58. S. B. Zhu, T. G. Xu, H. B. Fu, J. C. Zhao and Y. F. Zhu, *Environ. Sci. Technol.* 2007, **41**, 6234-6239.
59. H. B. Fu, T. G. Xu, S. B. Zhu and Y. F. Zhu, *Environ. Sci. Technol.*, 2008, **42**, 8064-8069.
60. V. Apostolopoulou, J. Vakros, C. Kordulis and A. Lycourghiotis, *Colloids Surf., A*, 2009, **349**, 189-194.
61. M. Q. Yang, N. Zhang and Y. J. Xu, *ACS Appl. Mater. Interfaces*, 2013, **5**, 1156-1164.
62. J. G. Yu, T. T. Ma, G. Liu and B. Cheng, *Dalton Trans.*, 2011, **40**, 6635-6644.
63. X. Zhao, H. J. Liu, Y. L. Shen and J. H. Qu, *Appl. Catal., B*, 2011, **106**, 63-68.
64. Z. D. Meng, L. Zhu and W. C. Oh, *J. Ind. Eng. Chem.*, 2012, **18**, 2004-2009.
65. G. Li, B. Jiang, X. Li, Z. Lian, S. Xiao, J. Zhu, D. Zhang and H. Li, *ACS Appl. Mater. Interfaces*, 2013, **5**, 7190-7197.

Table 1: The adhesion energy (E_{ad}), band gap E*g*(eV), mean distance (d) of optimized $C_{20}/Ag_3PO_4(100)$, $Li@C_{20}/Ag_3PO_4(100)$, $C_{26}/Ag_3PO_4(100)$, and $Li@C_{26}/Ag_3PO_4(100)$ composites.

Structure	E_{ad} (eV)	E_g (eV)	d (Å)	Bader Charge (e)	
				Ag_3PO_4	C/Li@C
$C_{20}/Ag_3PO_4(100)$	-2.15	1.92	3.06	-0.16	0.16
$Li@C_{20}/Ag_3PO_4(100)$	-0.76	2.04	3.07	-0.16	0.16
$C_{26}/Ag_3PO_4(100)$	-2.39	0.78	2.62	0.04	-0.04
$Li@C_{26}Ag_3PO_4(100)$	-0.78	0.66	2.67	0.08	-0.08

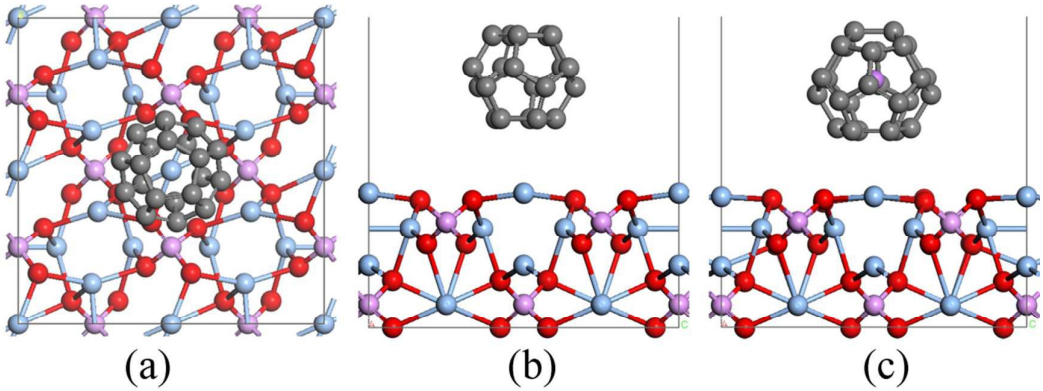

Figure 1: The (a) top and (b) side view of the simulating interface between C_{20} and the cubic $Ag_3PO_4(100)$ surface model, (c) side view of the simulating interface between $Li@C_{26}$ and the cubic $Ag_3PO_4(100)$ surface model. Gray, Red, purple, blue and deep purple spheres represent C, O, P, Ag and Li atoms, respectively.

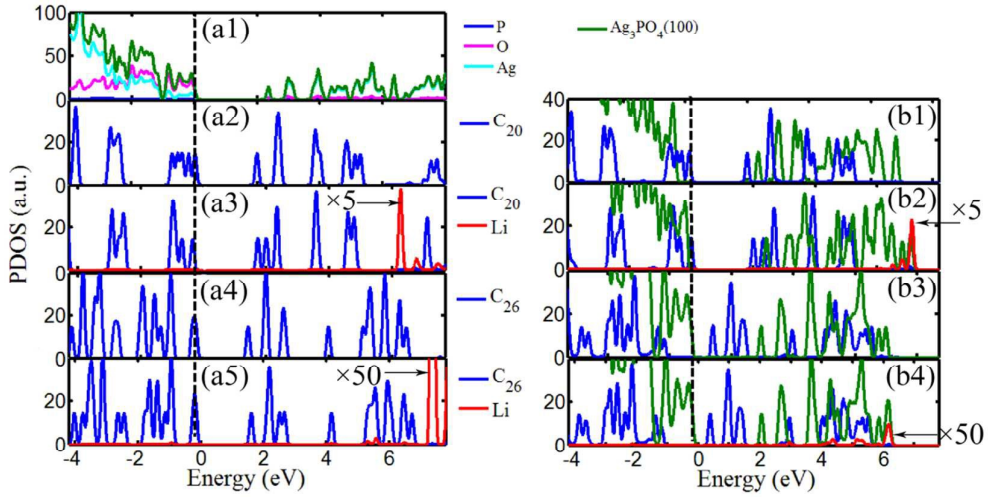

Figure 2: DOS for (a1-a5) pure $Ag_3PO_4(100)$ surface, C_{20}, $Li@C_{20}$, C_{26}, $Li@C_{26}$; (b1-b4) $C_{20}/Ag_3PO_4(100)$, $Li@C_{20}/Ag_3PO_4(100)$, $C_{26}/Ag_3PO_4(100)$, $Li@C_{26}/Ag_3PO_4(100)$ composites, respectively. The Fermi level is set to zero energy.

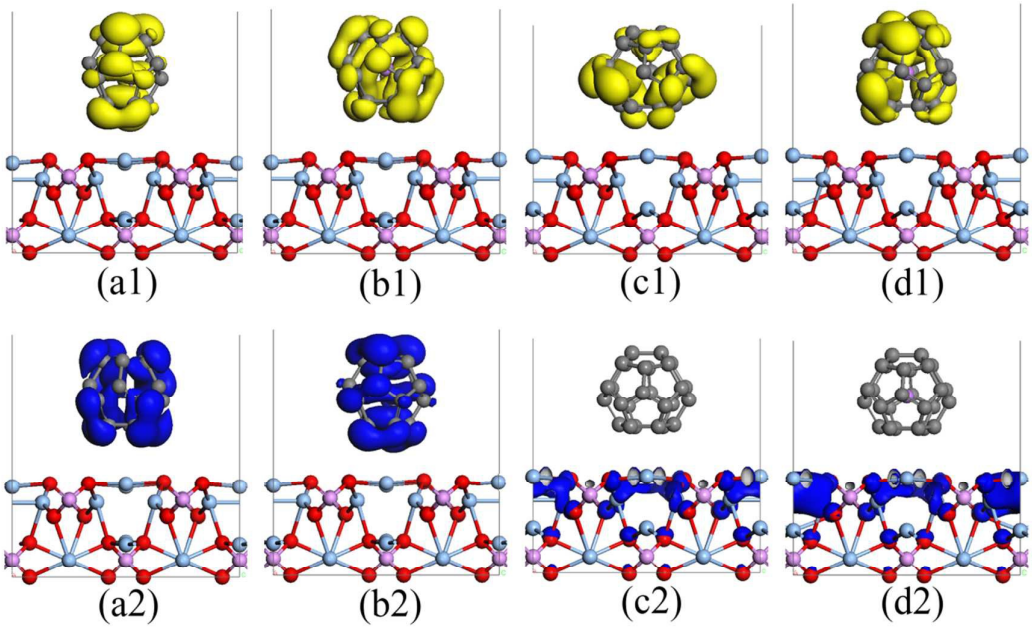

Figure 3: Maps of the electron and hole density distributions for the HOL (a1-d1) and LUL (a2-d2) for the hybrid C_{20}/Ag_3PO_4, $Li@C_{20}/Ag_3PO_4$, C_{26}/Ag_3PO_4, and $Li@C_{26}/Ag_3PO_4$, respectively. The isovalue is 0.004 e/Å^3. Here, HOL and LUL are determined by the highest-occupied and lowest-unoccupied levels, respectively.

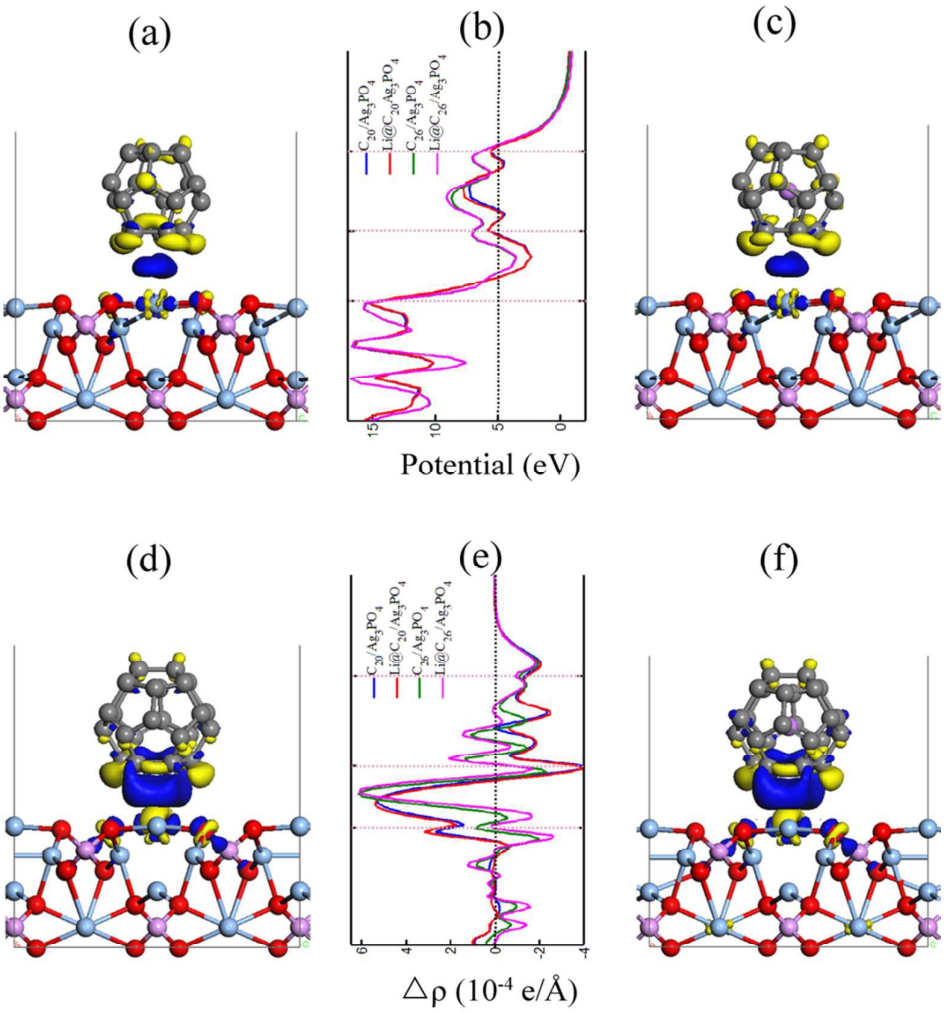

Figure 4: 3D Charge density differences for (a) $C_{20}/Ag_3PO_4(100)$, (c) $Li@C_{20}/Ag_3PO_4(100)$, (d) $C_{26}/Ag_3PO_4(100)$, (f) $Li@C_{26}/Ag_3PO_4(100)$ composites. The blue and yellow represent charge accumulation and depletion, respectively. The isovalue is 0.004 e/Å^3. (b) Profile of the planar averaged self-consistent electrostatic potential for the C_{20} ($Li@C_{20}$, C_{26}, $Li@C_{26}$)/$Ag_3PO_4(100)$ as a function of position in the z-direction. (e) Profile of the planar averaged charge density difference for the C_{20} ($Li@C_{20}$, C_{26}, $Li@C_{26}$)/$Ag_3PO_4(100)$ as a function of position in the z-direction. The horizontal dashed line from up to down indicates the location of the top of the C atoms, the bottom C atoms, the top layer of the $Ag_3PO_4(100)$, respectively.

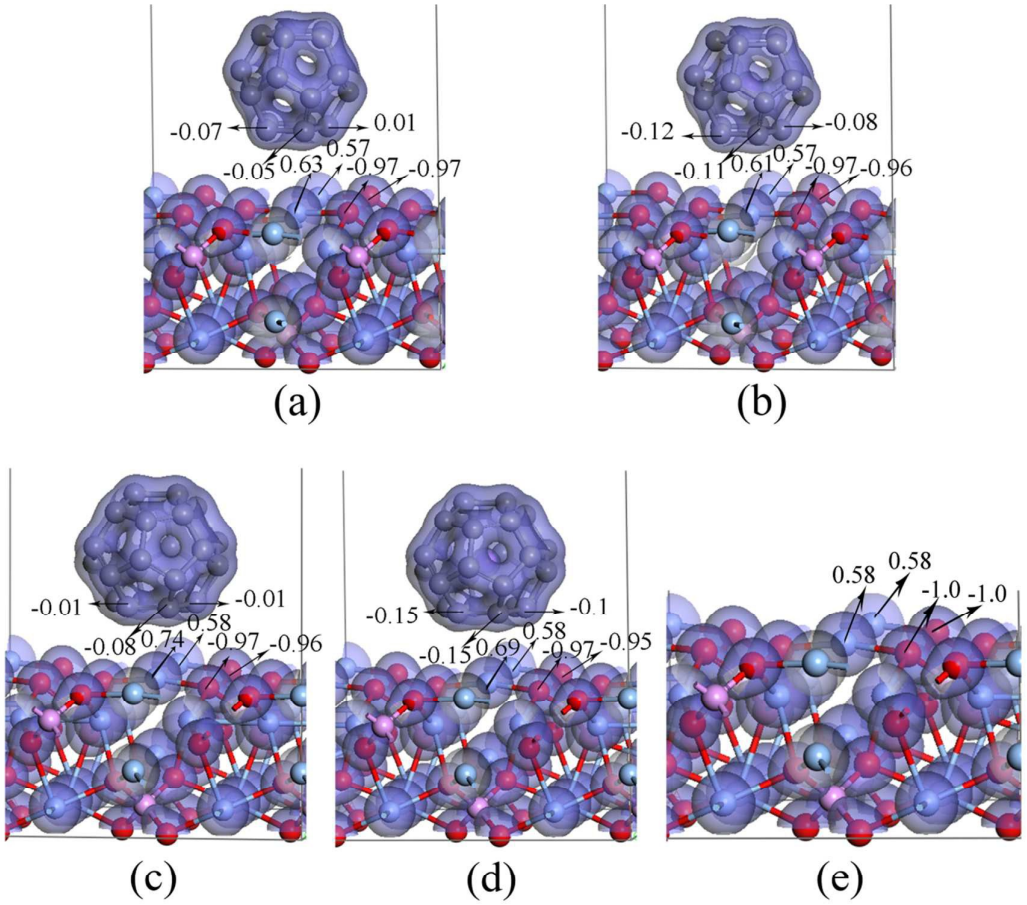

Figure 5. Charge distribution maps of (a) $C_{20}/Ag_3PO_4(100)$ and (b) $Li@C_{20}Ag_3PO_4(100)$ and (c) $C_{26}/Ag_3PO_4(100)$ and (d) $Li@C_{26}/Ag_3PO_4$ (100), (e) $Ag_3PO_4(100)$, with a isovalue of 0.7 e/Å^3. Gray, red, purple, deep purple and blue spheres represent C, O, P, Li and Ag atoms, respectively.

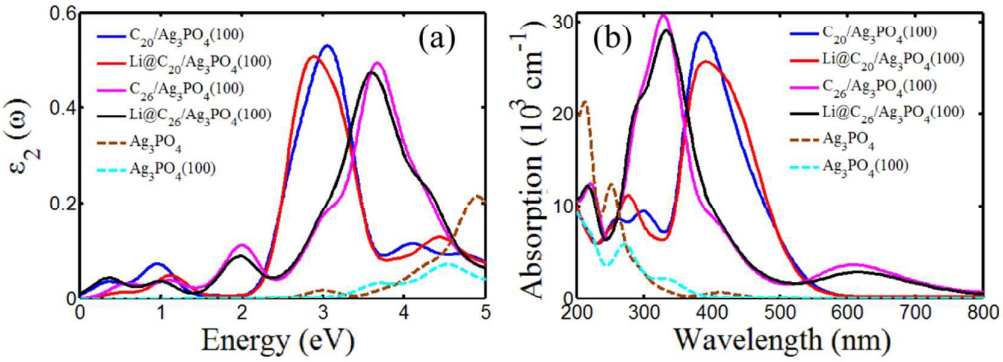

Figure 6: Calculated (a) imaginary part of the dielectric function and (b) absorption spectra of the $C_{20}/Ag_3PO_4(100)$ (blue solid line), $Li@C_{20}Ag_3PO_4(100)$ (red solid line), $C_{26}/Ag_3PO_4(100)$ (rose red solid line), $Li@C_{26}/Ag_3PO_4(100)$ (black solid line), bulk Ag_3PO_4 (brown dash line), and the cubic $Ag_3PO_4(100)$ surface (wathet blue dashed line) for the polarization vector perpendicular to the surface.